THE JOURNAL OF BIOLOGICAL CHEMISTRY VOL. 291, NO. 4, pp. 1692–1702, January 22, 2016

Novel Structural Components Contribute to the High Thermal Stability of Acyl Carrier Protein from *Enterococcus faecalis**

Received for publication, July 8, 2015, and in revised form, November 16, 2015 Published, JBC Papers in Press, December 2, 2015, DOI 10.1074/jbc.M115.674408

Young-Guen Park[‡], Min-Cheol Jung[‡], Heesang Song[‡], Ki-Woong Jeong[‡], Eunjung Bang[§], Geum-Sook Hwang[§], and Yangmee Kim[‡1]

From the [‡]Department of Bioscience and Biotechnology and the Bio/Molecular Informatics Center Konkuk University, Seoul 143-701, Korea and the [§]Western Seoul Center, Korea Basic Science Institute, Seoul 120-140, Korea

Enterococcus faecalis **is a Gram-positive, commensal bacterium that lives in the gastrointestinal tracts of humans and other mammals. It causes severe infections because of high antibiotic resistance.** ***E. faecalis*** **can endure extremes of temperature and pH. Acyl carrier protein (ACP) is a key element in the biosynthesis of fatty acids responsible for acyl group shuttling and delivery. In this study, to understand the origin of high thermal stabilities of** ***E. faecalis*** **ACP (*Ef*-ACP), its solution structure was investigated for the first time. CD experiments showed that the melting temperature of *Ef*-ACP is 78.8 °C, which is much higher than that of *Escherichia coli* ACP (67.2 °C). The overall structure of *Ef*-ACP shows the common ACP folding pattern consisting of four α-helices (helix I (residues 3–17), helix II (residues 39–53), helix III (residues 60–64), and helix IV (residues 68–78)) connected by three loops. Unique *Ef*-ACP structural features include a hydrophobic interaction between Phe^{45} in helix II and Phe^{18} in the $\alpha_1\alpha_2$ loop and a hydrogen bonding between Ser^{15} in helix I and Ile^{20} in the $\alpha_1\alpha_2$ loop, resulting in its high thermal stability. Phe^{45}-mediated hydrophobic packing may block acyl chain binding subpocket II entry. Furthermore, Ser^{58} in the $\alpha_2\alpha_3$ loop in *Ef*-ACP, which usually constitutes a proline in other ACPs, exhibited slow conformational exchanges, resulting in the movement of the helix III outside the structure to accommodate a longer acyl chain in the acyl binding cavity. These results might provide insights into the development of antibiotics against pathogenic drug-resistant** ***E. faecalis*** **strains.**

Fatty acids are the central building blocks of life. Fatty acid synthase (FAS)[2] is an important pathway for the production of fatty acids and plays an important role in the formation of cell membranes, energy storage compounds, and messenger substances. Fatty acids also act as post-translational protein modifiers and modulate gene expression (1). In nature, there are two types of FAS systems, type I and type II. Type I FAS systems are found in mammals and fungi; this system is composed of a single polypeptide chain of covalently linked domains that forms large multienzyme complexes (2, 3). In contrast, type II FAS systems are found in bacteria and eukaryotic organelles and are dissociated so that all proteins are expressed as individual enzymes (4–7). Given the vast difference in these two systems between humans and bacteria, there has been a conscious effort to target FAS in bacteria through novel antibiotics.

Acyl carrier proteins (ACPs) are small (9-kDa) acidic proteins that are essential for numerous biosynthetic pathways that play a role in acyl group transfer. ACPs are also required for a variety of other mechanisms that require acyl group transfer steps, such as polyketide antibiotic synthesis, lipopolysaccharides, rhizobial modulation signaling factors, lipoteichoic acids, and prohemolysin toxin activation (8–11). However, the biosynthesis of fatty acids is the predominant role of ACP. ACPs are highly conserved proteins typically consisting of 70–100 residues and are essential components in type I and type II FAS systems (12, 13), which shuttle bound fatty acyl intermediates in a hydrophobic pocket to facilitate interaction with various enzyme partners (14). Therefore, ACP is believed to be a mobile protein, and its flexibility is essential for its interaction with functionally different enzyme partners.

Enterococci cause serious infections in animals and humans. Almost all enterococcal infections are caused by *Enterococcus faecalis* (15). *E. faecalis* is a bacterium that inhabits the gastrointestinal tracts of humans and other mammals. It also commonly resides in soil, water sewage, and contaminated food. Furthermore, *E. faecalis* can tolerate oxidative stress and dry conditions and can grow in 6.5% NaCl, 40% bile salts, and at a broad range of pH (16, 17). In particular, *E. faecalis* is able to grow in a high temperature range from 10 to 40 °C and can also survive at 85 °C; this thermotolerance can allow it to survive in hospital laundries (16, 18). *E. faecalis* also has a high resistance to salinity, detergents, antibiotics drugs, sodium azide, and bile acids, which kill most microorganisms (19, 20). *E. faecalis* can survive in patient clothing for over 11 days, which is a relatively long period (21). *E. faecalis* is able to cause life-threatening infections in humans, especially in the hospital environment (22–24). Furthermore, *E. faecalis* has the ability to become resistant to vancomycin, penicillins, cephalosporins, and ami-

* This work was supported by Basic Science Research Program Grant 2013R1A1A2058021 and Priority Research Centers Program Grant 2009-0093824 through the National Research Foundation of Korea, funded by the Ministry of Education, Science, and Technology. The authors declare that they have no conflicts of interest with the contents of this article.

The atomic coordinates and structure factors (code 2N50) have been deposited in the Protein Data Bank (http://wwpdb.org/).

[1] To whom correspondence should be addressed: Dept. of Bioscience and Biotechnology, Konkuk University, Seoul 143-701, South Korea. Tel.: 822-450-3421; Fax: 822-447-5987; E-mail: ymkim@konkuk.ac.kr.

[2] The abbreviations used are: FAS, fatty acid synthase; ACP, acyl carrier protein; *Ef*-ACP, *Enterococcus faecalis* ACP; *Ec*-ACP, *Escherichia coli* ACP; AcpS, holo-ACP synthase; hNOE, heteronuclear Overhauser effect; HSQC, heteronuclear single quantum coherence spectroscopy; PDB, Protein Data Bank.

noglycosides through mutation (20, 25–27). Vancomycin-resistant enterococci in particular are important etiologic agents of nosocomial infections and colonization in hospitalized patients (28). Because FAS proteins of antibiotic-resistant strains can be potential targets while designing novel antibiotics, we have developed potent inhibitors for FabH from methicillin-resistant *Staphylococcus aureus* and vancomycin-resistant *E. faecalis*, which is a condensing enzyme in bacterial FAS (29, 30).

The structures of various kinds of type II ACPs have been studied. Solution structures of ACPs from *Escherichia coli* (31, 32), *Bacillus subtilis* (33), *Mycobacterium tuberculosis* (34), *Vibrio harveyi* (32), *Helicobacter pylori* (35), *Borrelia burgdorferi* (36), and *Plasmodium falciparum* (37) have been determined by NMR spectroscopy. Also, NMR structures of ACP domains of various type I FAS have been studied (38–40). Structural studies of ACPs have revealed that ACPs are composed of four helix bundles and a prosthetic group attached to a conserved Ser residue located in helix II. Type II ACPs have high sequence similarity; in particular, the acidic residues in helix II that are important in interactions with FAS enzymes and DSL motifs are highly conserved (41). However, despite such considerable sequence similarity, the thermal stability of *E. faecalis* ACP (*Ef*-ACP) is much higher than that of other ACPs. In this study, to understand the origin of the thermal stability of *Ef*-ACP, we determined for the first time the tertiary structure of ACP from *E. faecalis*. In this work, we measured the melting temperatures (T_m) of wild type and mutant *Ef*-ACPs using CD experiments and compared these with the T_m of other ACPs to understand the origin of the high thermal stability of *Ef*-ACP. We also monitored amide exchange rates to understand the stability of the structural elements in *Ef*-ACP. To investigate the importance of *Ef*-ACP structural flexibility, the dynamic properties of *Ef*-ACP were assessed by measuring spin relaxation rates and were correlated with its thermal stability in comparison with those of other ACPs.

Experimental Procedures

Cloning, Expression, and Purification of Ef-ACP—The *acpP* gene encoding ACP was amplified from *E. faecalis* genomic DNA. A restriction site (NdeI for the sense primer and BamHI for the antisense primer) was attached to the 5′-end of each primer to facilitate cloning. PCR was performed with 35 cycles of denaturation for 1 min at 95 °C, annealing for 1 min at 54 °C, and elongation for 1 min at 72 °C. The resulting product was cloned into the NdeI and BamHI sites of the pET-11a vector (Novagen, Madison, WI). The ligation mixture was transformed into *E. coli* DH5α competent cells. For expression of H/^{15}N/^{13}C-labeled ACP, plasmids encoding ACP were transformed in *E. coli* BL21 (DE3) cells and then grown overnight as subcultures and isolated by centrifugation. The resulting cell pellet was mixed with 100 ml of M9 minimal media containing 1 g/liter $^{15}NH_4Cl$ and [^{13}C]glucose (Cambridge Isotope Laboratories, Andover, MA) and 100 mg/liter ampicillin and grown to an A_{600} between 0.8 and 1.0. This culture was added to 1 liter of the same minimal media, and protein expression was induced by adding isopropyl β-D-thiogalactopyranoside at an A_{600} of 0.8–1.0 and incubating at 25 °C for ~24 h. *Ef*-ACP was purified using a HiTrap^{TM} QFF and Hiload 16/60 Superdex 75 column. The holo-ACPs were produced by enzymatic acylation of apo-ACPs using *E. coli* holo-ACP synthase (AcpS) and coenzyme A (Sigma-Aldrich) (42), and the holo-ACP was separated for apo-ACP using a Resource Q column. These samples were analyzed by 20% native gel electrophoresis followed by Coomassie staining to distinguish the apo- and holo-ACPs (43).

CD Measurements of Purified ACP—CD measurements were performed in a J810 spectropolarimeter (Jasco, Tokyo, Japan) using a cell with a 1-mm path length. The CD spectra of *Ef*-ACP in 25 mM MES buffer, pH 6.1, containing 5 mM $CaCl_2$ and 5 mM dithiothreitol (DTT) at 25 °C were measured at 0.1-nm intervals from 200 to 250 nm. The protein concentration was 50 μM, and data from five scans were averaged and smoothed using J810 software. CD data were shown as the mean residue ellipticity (θ) in degrees cm^2 dmol^{-1}. Protein T_m values were determined from a series of CD spectra obtained from 15 to 100 °C.

NMR Analysis and Structure Calculation—All NMR experiments were performed at 25 °C on a Bruker Avance 700-, 800-, and 900-MHz spectrometer at the Korea Basic Science Institute. All of the spectra were processed with NMRPipe (44) and analyzed using Sparky (45). The compound 2,2-dimethyl-2-silapentane-5-sulfonate was used as an internal standard. *Ef*-ACP samples were prepared at 1 mM concentration in 25 mM MES buffer, pH 6.1, containing 5 mM $CaCl_2$, 5 mM DTT, 0.02% NaN_3, and 10% D_2O. For backbone assignments, HNCACB and CBCA(CO)NH triple resonance spectra were recorded, and assignments of aliphatic side chains were from HCCH-TOCSY and CCH-TOCSY spectra.

Anisotropic orientational restraints were obtained from ^{15}N-labeled ACP with 40% strained polyacrylamide gel and compared with ^{15}N-labeled ACP lacking polyacrylamide gel. $^1J_{NH}$ coupling measurements were performed using the IPAP-HSQC method (46) with one-bond ^{15}N–^{1}H residual dipolar couplings taken to be the difference between $^1J_{NH}$ measurements in isotropic and aligned samples. TALOS+ (47) was used in deriving backbone dihedral angle restraints (Φ and Ψ) from $^1H\alpha$, ^{15}N, $^{13}C\alpha$, $^{13}C\beta$, and $^{13}C'$ chemical shift values. The NOE restraints were obtained from ^{15}N-edited NOESY-HSQC, ^{13}C-edited NOESY-HSQC spectra. CYANA version 3.9 (48, 49) was used for automatic NOESY peak assignments and structure calculations. NOESY peaks assigned automatically by CYANA were used as a guide to further refine the structure. Residual dipolar coupling refinement was performed using CYANA version 3.9. The analysis of Ramachandran plots for the 20 lowest energy structures was carried out using PROCHECK (50). The protein structures were represented using PyMOL and MOLMOL (51). The chemical shifts, coordinates, and NMR-derived constraints have been deposited in the Biological Magnetic Resonance Bank (accession number 25688; Protein Data Bank (PDB) entry 2N50).

Spin Relaxation Experiments—The ^{15}N-labeled samples of ACPs contained 0.5 mM protein in 25 mM MES (pH 6.1), 5 mM DTT, 0.02% NaN_3, and 10% D_2O in the presence of 5 mM $CaCl_2$ and in the absence of $CaCl_2$. All NMR experiments were performed at 25 °C on a Bruker Advance 700-MHz spectrometer. The longitudinal relaxation rates (R_1) were measured with relaxation delays of 0.002 (×2), 0.045, 0.100, 0.200, 0.315 (×2),

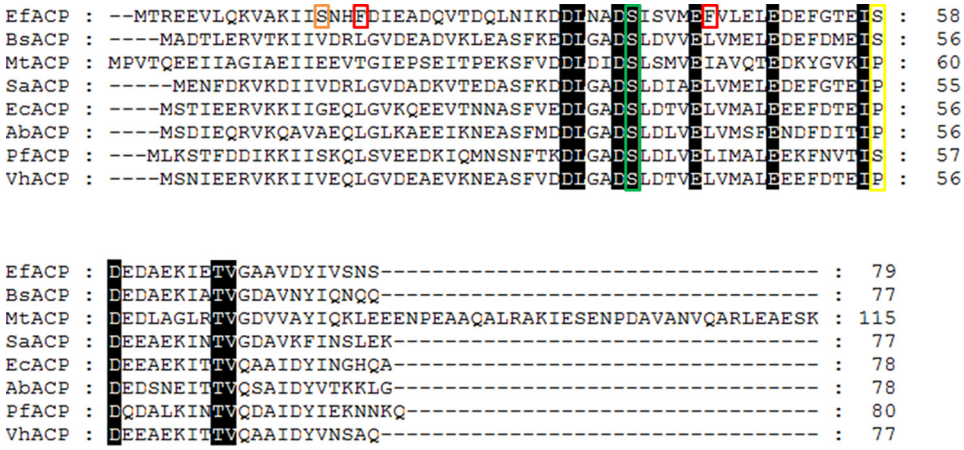

FIGURE 1. **Sequence alignment of ACP.** Sequence alignment of the *Ef*-ACP protein with three Gram-positive homologues (*B. subtilis* ACP (*BsACP*), *M. tuberculosis* ACP (*MtACP*), and *S. aureus*-ACP (*SaACP*)) and four Gram-negative bacterial homologues (*E. coli* ACP (*EcACP*), *A. baumanni* ACP (*AbACP*), *P. falciparum* ACP (*PfACP*), and *V. harveyi* ACP (*VhACP*)). The conserved residues with 100% identity are shown in *black*. The prosthetic group attachment site, which is highly conserved (Ser[39] in *Ef*-ACP) is marked by a *green box*. Unique features of *Ef*-ACP are marked with *orange* (Ser[15]), *red* (Phe[18] and Phe[45]), and *yellow boxes* (Ser[58]). The residues *marked* with a *red box* form hydrophobic interactions with each other and are found only in *Ef*-ACP. The residues in the *yellow box* are composed of a proline in the $\alpha_2\alpha_3$ loop of most ACPs, but *Ef*-ACP carries a serine residue in the $\alpha_2\alpha_3$ loop.

0.550, 0.800, and 1.000 s. The transverse relaxation rates (R_2) were measured with relaxation delays of 0 (×2), 0.01696, 0.03328, 0.05088 (×2), 0.0848, 0.11872, 0.18656, and 0.28832 s (52). The heteronuclear cross-relaxation rate was measured by heteronuclear Overhauser effect (hNOE) experiments by using the interleaving pulse sequences with and without proton saturation. The recycle delay and proton saturation times in the hNOE measurement were 4.5 and 3.0 s, respectively. All relaxation spectra were acquired and analyzed as described in our previous reports (53, 54). hNOE was calculated from the ratio of peak heights with and without proton saturation pulses. R_1 and R_2 rates were determined by fitting the peak heights using Sparky.

Site-directed Mutagenesis of Ef-ACP—Mutagenesis of the *Ef*-ACP variant was performed using a Muta-Direct™ site-directed mutagenesis kit (Intron Biotechnology, Seongnam, Korea), and plasmid constructs of *Ef*-ACP variants containing mutations at positions His[17], Phe[18], Phe[45], and Phe[53] were cloned by PCR using the synthetic oligonucleotide primer pairs 5′-ATT TCA AAC GCG TTT GAT ATT GAA GCG-3′ (forward) and 5′-CGC TTC AAT AAA CGC GTT TGA GAT ATT-3′ (reverse) for H17A, 5′-AGC GTA ATG GAG GCG GTT TTA GAA CTT G-3′ (forward) and 5′-CAA GTT CTA AAA CCG CCT CCA TTA CGC T-3′ (reverse) for F45A, 5′-GAT TAT CTC AAA CCA CGC GGA TAT TGA AGC GGA TC-3′ (forward) and 5′-GAT CCG CTT CAA TAT CCG CGT GGT TTG AGA TAA TC-3′ (reverse) for F18A, and 5′-ACT TGA AGA TGA AGC GGG AAC AGA GAT TT-3′ (forward) and 5′-AAA TCT CTG TTC CCG CTT CAT CTT CAA GT-3′ (reverse), using *Ef*-ACP DNA as a template. PCR amplifications were performed using 10 fmol of template DNA, 1 μM each primer, 0.2 mM each deoxyribonucleotide triphosphate, and 2 μM *Taq* polymerase under the following thermocycling conditions: 25 cycles of denaturation at 95 °C (30 s), annealing at 54 °C (1 min), and primer elongation at 72 °C (1 min).

Hydrogen/Deuterium Exchange Experiments—*Ef*-ACP samples were prepared at a concentration of 0.5 mM protein in 25 mM MES buffer, pD 6.1, 5 mM DTT, and 0.02% NaN_3 containing 5 mM $CaCl_2$ and in the absence of $CaCl_2$. Data acquisition was started ~5 min after the addition of D_2O to the protein. A series of heteronuclear single quantum coherence spectroscopy (HSQC) spectra were acquired every 10 min using two scans and 1024 × 256 data points for 10 h; after 4 days, additional HSQC spectra were acquired using the same conditions. Decay of amide proton signal as a function of time was measured by the decrease in peak height. To determine the exchange rate constant of protein, decay curves were fit using a single-exponential function ($I = I_0 \exp(-k_{ex}t) + C$), where I represents the NH resonance intensities as a function time (t), I_0 is initial intensity, and k_{ex} is exchange rate of protein. The protection factor was calculated by the comparison of measured hydrogen/deuterium exchange rates for protein (k_{prot}) with the rates for the random coil conformation (k_{rc}) (55).

Results

Thermal Stability of the Ef-ACP—*Ef*-ACP is a highly acidic protein with a pI value of 4.2 with 21 acidic residues. As shown in Fig. 1, sequence alignments revealed that type II bacterial ACPs have high sequence similarities with *Ef*-ACP. ACPs have a strictly conserved serine residue where the 4′-phosphopantetheine prosthetic group is attached (marked with a *green box* in Fig. 1). Some distinct features were noted in the sequence of *Ef*-ACP. All ACPs have a conserved aromatic residue at the end of helix II, whereas *Ef*-ACP has an additional Phe (Phe[45]) in the middle of helix II. In addition, *Ef*-ACP has Phe[18] at the beginning of loop I, resulting in stable hydrophobic interactions with Phe[45] (marked with a *red box* in Fig. 1). There are proline residues in the $\alpha_2\alpha_3$ loops connecting helix II and helix III in most ACPs, including *Ec*-ACP (Pro[55]), whereas in *Ef*-ACP, this is replaced with a serine residue (Ser[58]), providing more flexibility (marked with a *yellow box* in Fig. 1). As shown in Fig. 1, all ACPs are highly acidic; divalent cations reduce the severe electrostatic repulsions between the acidic residues in ACP. *Ef*-ACP has 11 Glu and 10 Asp residues, whereas *Ec*-ACP has 14 Glu and 6 Asp. It has been reported previously that *Ec*-ACP has

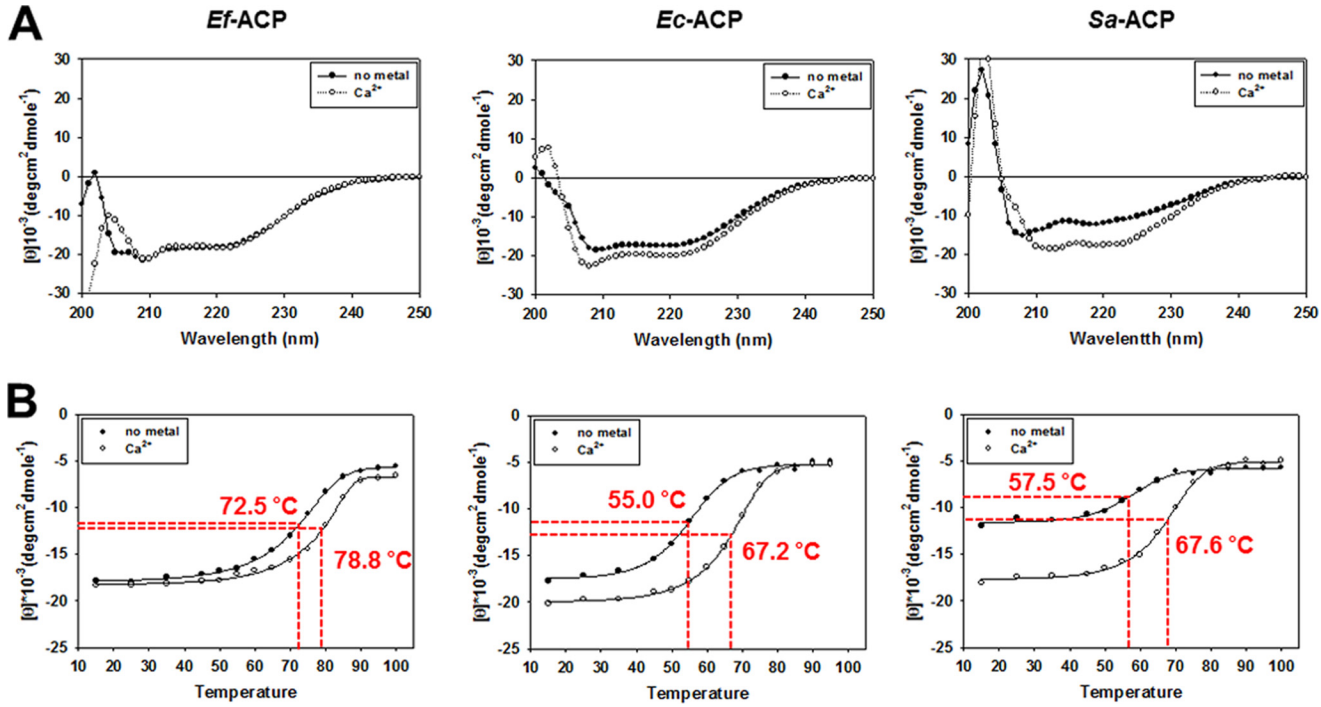

FIGURE 2. **CD spectra of *Ef*-ACP, *Ec*-ACP, and *S. aureus* ACP (*Sa*-ACP).** *A*, CD spectrum of ACPs in the presence of Ca^{2+} (○) and in the absence of Ca^{2+} (●) at 25 °C. *B*, temperature-induced folding change of ACPs as monitored by changes of ellipticity at 222 nm. The *red dotted line* indicates the T_m point of each graph.

two metal binding sites: site A consisting of Glu^{30}, Asp^{35}, and Asp^{38} and site B consisting of Glu^{47}, Asp^{51}, Glu^{53}, and Asp^{56} (56).

Despite high similarities between *Ec*-ACP and *Ef*-ACP, the melting temperature of *Ef*-ACP was markedly different from that of *Ec*-ACP. The CD spectrum of *Ef*-ACP showed double minima at 205 and 222 nm, which are characteristic of an α-helical structure (Fig. 2*A*). Analysis of the thermal denaturation curves obtained from 15 to 100 °C showed that the T_m of *Ef*-ACP with $CaCl_2$ is 6.3 °C higher than that in the absence of Ca^{2+} ions (Fig. 2*B*). Table 1 lists the T_m values of various ACPs. We measured the T_m values of *Ec*-ACP and *S. aureus* ACP, and compared these with that of *Ef*-ACP by CD experiments. The T_m of *Ec*-ACP in the presence of Ca^{2+} was 67.2 °C, much higher than 55.0 °C, the T_m of *Ec*-ACP in the absence of metal ions. The T_m of *S. aureus* ACP in the presence of Ca^{2+} was 67.6 °C, which was relatively lower than those of other ACPs, whereas the T_m of *S. aureus* ACP in the absence of metal ions was 57.5 °C, an additional 10.1 °C lower than that with Ca^{2+}. For *Ec*-ACP, as listed in Table 1, we compared our data with the previously reported T_m measured by differential scanning calorimetry and found that the buffer condition as well as the measurement methods resulted in a small difference in T_m (57). However, both results confirmed that the T_m of *Ec*-ACP in the presence of Ca^{2+} was >12 °C higher than that of *Ec*-ACP in the absence of metal ions. Also, it has been reported that *V. harveyi* ACP has an α-helical structure with a T_m value of 66.4 °C in the presence of Ca^{2+}, whereas this protein is unfolded in the absence of Ca^{2+} (58). The measurement of melting temperatures implied that *Ef*-ACP has much higher thermal stability than does other ACPs. Therefore, in this study, we investigated the key factors that stabilize the specific conformations of *Ef*-ACP.

Chemical Shift Perturbations of Apo- and Holo-Ef-ACP—To investigate the effect of the prosthetic group binding in *Ef*-ACP, chemical shift perturbations upon conversion of the apo- to the holo-form were studied by comparing the ^{1}H-^{15}N HSQC spectra of holo- and apo-ACPs (Fig. 3*A*). This analysis showed that the chemical shifts of apo- and holo-*Ef*-ACPs are very similar. Upon this conversion by covalent modification of Ser^{39} by a phosphopantetheine prosthetic group, large chemical shift changes (>0.1 ppm) were observed near the prosthetic group binding site at Ser^{39} and Ile^{40}. The results are in reasonable agreement with those of the most perturbed residues reported for phosphopantetheinylation of *B. subtilis* ACP, *Ec*-ACP, and *M. tuberculosis* ACP (33, 34, 59). In addition, the residues Ala^{37}, Asp^{38}, Ser^{41}, Val^{42}, Met^{43}, and Glu^{44} near the site of prosthetic group attachment undergo chemical shift changes ($0.03 < ppm < 0.1$), as indicated with different *colors* on the *ribbon structure* of holo-*Ef*-ACP (Fig. 3*B*). Furthermore, residues such as Ile^{57}, Ser^{58}, Ile^{65}, and Ala^{70}, which form a hydrophobic cleft and are affected by the prosthetic group, show chemical shift perturbations ($0.03 < ppm < 0.05$) between the apo- and holo-forms.

The Structure of Ef-ACP—To understand the relationship between the structure and the thermal stability of *Ef*-ACP, we determined the tertiary structure of *Ef*-ACP. The three-dimensional structure of *Ef*-ACP was calculated based on NMR constraints. A total of 1510 NOE distance restraints, 148 backbone torsion angle restraints, and 72 orientational restraints were identified for *Ef*-ACP (Table 2). The patterns of short and medium range NOEs observed in the ^{15}N and ^{13}C HSQC-NOESY spectra of *Ef*-ACP indicate that *Ef*-ACP possesses three relatively long helices and one short helix. In the final structural calculations, a total of 100 structures for ACP were calculated using the program CYANA, and 20 structures with the lowest

TABLE 1
Melting temperatures of ACPs

	Buffer conditions	Metal	T_m
			℃
Ef-ACP	25 mM MES (pH 6.1), 5 mM DTT	None[a]	72.5[b]
		5 mM $CaCl_2$	78.8[b]
Ec-ACP	25 mM MES (pH 6.1), 5 mM DTT	None[a]	55.0[b]
		5 mM $CaCl_2$	67.2[b]
S. aureus ACP	25 mM MES (pH 6.1), 5 mM DTT	None[a]	57.5[b]
		5 mM $CaCl_2$	67.6[b]
Ec-ACP	50 mM Sodium acetate (pH 6.1), 0.5 mM DTT	None[a]	52.7 (57)[c]
		8.4 mM $CaCl_2$	64.3 (57)[c]
V. harveyi ACP	5 mM Hepes (pH 6.5)	None[a]	Unfolded (58)
		2 mM $CaCl_2$	66.4 (58)[c]

[a] T_m was measured in the absence of metal ion.
[b] T_m was measured by CD spectroscopy.
[c] T_m was measured by differential scanning calorimetry.

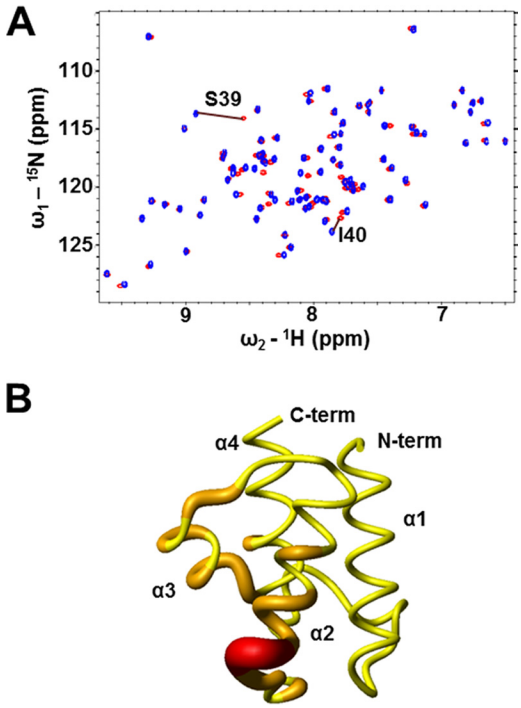

FIGURE 3. **NMR data of apo- and holo-ACP.** *A*, overlay of the ^{1}H-^{15}N HSQC spectra of apo- (*red*) and holo-ACP (*blue*). *B*, chemical shift change value ranges induced by 4′-phosphopantetheine prosthetic group modification of apo-ACP are indicated in *various colors* in *tubular drawings*. Residues with ppm >0.03 are shown with *graduated larger ribbon diameters*. *N-term* and *C-term*, N and C termini, respectively. *Red*, >0.1 ppm; *orange*, 0.03 < ppm < 0.1; *yellow*, <0.03 ppm. Chemical shift perturbations were calculated using the equation, $\Delta\delta_{av} = (0.5(\Delta\delta(^1H^N)^2 + (0.2\Delta\delta(^{15}N))^2))^{1/2}$.

target functions were selected and superimposed (Fig. 4*A*). The root mean square deviations of *Ef*-ACP were 0.18 ± 0.02 Å for backbone (N, Cα, and C′) atoms, and 0.66 ± 0.05 Å for all heavy atoms of residues 2–79, respectively. The solution structures of *Ef*-ACPs consisted of four α-helices where α_1 (Arg^3–His^{17}), α_2 (Ser^{39}–Phe^{53}), α_3 (Glu^{60}–Lys^{64}), and α_4 (Val^{68}–Asn^{78}) were connected by three loops (Fig. 4*B*). Helix III was shorter relative to the other helices. A shorter $\alpha_2\alpha_3$ loop (Gly^{54}–Asp^{59}) connected helix II to III, and a 3-residue $\alpha_3\alpha_4$ loop (Ile^{65}–Thr^{67}) linked helices III and IV.

The α-helices of *Ef*-ACP have amphipathic character. Many of the long range NOEs involved in packing of the helical bundle arose from the contacts between the hydrophobic side chains, corresponding to residues Val^6, Val^{10}, and Ile^{13} in helix I; Phe^{18} and Ile^{31} in the $\alpha_1\alpha_2$ loop; Phe^{45}, Val^{46}, Leu^{49}, and Phe^{53} in helix II; Ile^{57} in the $\alpha_2\alpha_3$ loop; Ala^{61} in helix III; and Ala^{71}, Tyr^{74}, and Ile^{75} in helix IV. These residues form the hydrophobic cavity of *Ef*-ACP to accommodate the growing acyl chain, in which hydrophobic interactions between these residues stabilize the global fold of *Ef*-ACP. Unusually, *Ef*-ACP has three phenylalanines, Phe^{18}, Phe^{45}, and Phe^{53}, which play an important role in hydrophobic packing of the helical bundle, as shown in Fig. 4, *B* and *C*, whereas *Ec*-ACP has only two phenylalanines, Phe^{28} and Phe^{50}. As commonly shown in most ACP structures, Val^6, Phe^{53}, and Ile^{75} at the top end of the hydrophobic cavity of ACP have close hydrophobic contacts with each other (Fig. 4*B*). Phe^{18} is located at the beginning of the first long loop and forms a hydrophobic interaction with Phe^{45} in helix II (Fig. 4*C*). We also noted a unique structural feature that stabilizes the flexible long $\alpha_1\alpha_2$ loop of *Ef*-ACP; the side chain oxygen of Ser^{15} and the backbone amide proton of Ile^{20} form a hydrogen bonding interaction (Fig. 4*D*). In addition, the backbone carboxyl group of Glu^{50} and the backbone amide proton of Thr^{55} form a hydrogen bonding interaction.

TABLE 2
Structural statistics and mean pairwise root mean squared deviations for the 20 lowest energy structures of *Ef*-ACP

Distance restraints	*Ef*-ACP
Total	1510
Intraresidual and sequential	752
Medium range	461
Long range	297
Dihedral angle restraints	148
Hydrogen bonds	44
Orientational restraints	72
Mean Cyana target function (+)	4.01 ± 0.03
Coordinate precision[a]	
Backbone (+)	0.18 ± 0.02
Heavy atom (Å)	0.66 ± 0.05
Ramachandran plot statistics (%)[b]	
Residues in most favored regions	82.9
Residues in additional allowed regions	17.1
Residues in generously allowed regions	0.0
Residues in disallowed regions	0.0

[a] The average root mean square deviation for the overall structure between the 20 structures calculated for *Ef*-ACP.
[b] Determined using the program PROCHECK (50).

Dynamics of Ef-ACP—Fast backbone dynamics on a picosecond-to-nanosecond time scale were studied by measuring the R_1, R_2, and hNOEs of *Ef*-ACP (Fig. 5). The average R_1, R_2, and hNOE values of *Ef*-ACP were 1.76 ± 0.027, 7.38 ± 0.24, and 0.79 ± 0.007 s^{-1}. The average R_2/R_1 ratio for *Ef*-ACP was 3.93, implying that *Ef*-ACP exists as monomer. Relaxation rates showed relatively uniform behavior across the protein

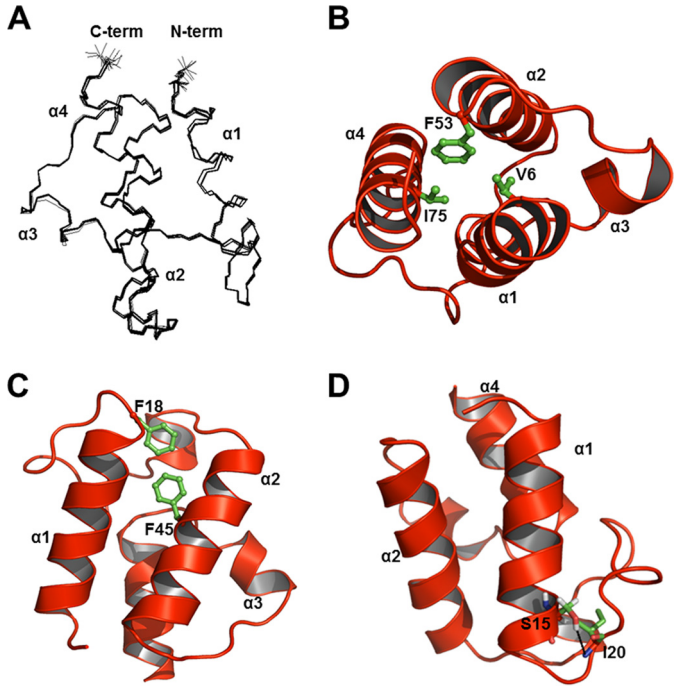

FIGURE 4. **Structure of *Ef*-ACP.** *A*, superposition of backbone (nitrogen, Cα, and C′) atoms of the 20 lowest energy structures of holo-*Ef*-ACP. All residues (positions 1–79) are shown, and N and C termini are *labeled* as *N-term* and *C-term*, respectively. *B*, hydrophobic contacts of Val^{6}, Phe^{53}, and Ile^{75} in holo-*Ef*-ACP. *C*, hydrophobic interactions between Phe^{18} and Phe^{45}. *D*, hydrogen bond interactions between Ser^{15} and Ile^{20} are depicted with *black dotted lines*. In *B–D*, all structures are represented as *schematic diagrams*, and each helix is *labeled* from $\alpha 1$ to $\alpha 4$. Each residue is depicted as *green sticks*.

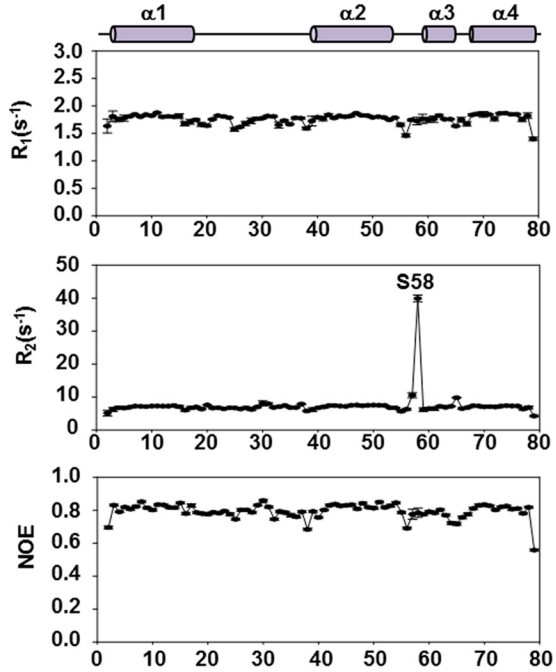

FIGURE 5. **Spin relaxation rates of *Ef*-ACP in the presence of Ca^{2+}.** Relaxation data of *Ef*-ACP were measured at 298 K. The values of R_1, R_2, and the steady-state heteronuclear NOEs are plotted as a function of the residue sequence number for *Ef*-ACP. *Above* the *plots*, the *solid* and *filled bars* represent the four helices of *Ef*-ACP.

sequence with the exception of the loop regions and the residues at the N and C termini. The R_2 values were uniform in all regions except for Ile^{57} and Ser^{58} in the $\alpha_2\alpha_3$ loop region. Ser^{58} in *Ef*-ACP corresponds to Pro^{55} in *Ec*-ACP, which forms the rigid bent structure right before helix III. Ile^{57} (10.51 ± 0.76 s^{-1}) and Ser^{58} (39.86 ± 1.04 s^{-1}) have high R_2 values, implying that they have conformational exchange caused by the relatively more flexible loop motions compared with those of Ile^{54} and Pro^{55} in *Ec*-ACP (59). As shown in Fig. 3*B*, these two residues show chemical shift perturbations (0.042 ppm in Ile^{57} and 0.037 ppm in Ser^{58}) induced by phosphopantetheine modification. These results imply that the Ile^{57} and Ser^{58} loop region might have a conformational exchange to generate enough room to accommodate the longer acyl chains.

The average hNOE values in the helix regions, α_1 (Arg^{3}–His^{17}), α_2 (Ser^{39}–Phe^{53}), α_3 (Glu^{60}–Lys^{64}), and α_4 (Val^{68}–Asn^{78}) were high, which implied structural rigidity: 0.81, 0.82, 0.77, and 0.81. Residues at each end of helix II, such as Asp^{38} and Glu^{56}, exhibited relatively lower hNOE values. Asp^{38} is located at the end of the long $\alpha_1\alpha_2$ loop region (Phe^{18}–Asp^{38}) near the prosthetic group binding sites, and Glu^{56} is at the flexible $\alpha_2\alpha_3$ loop region of *Ef*-ACP. Significantly reduced hNOE values were observed for the N and C termini because of the flexibilities of the terminal regions in protein structure. The hNOE value of Ser^{79} at the C terminus was not negative but was low because the peak for Val^{25} was overlapped with the peak for Ser^{79}. The hNOE values for the $\alpha_1\alpha_2$ loop are relatively high in consideration of its length, resulting from hydrogen bonds between Ser^{15} and Ile^{20}. Therefore, the structural rigidity and thermal stability of *Ef*-ACP resulted from the hydrophobic interactions between the residues forming the hydrophobic cleft of *Ef*-ACP.

Hydrogen/Deuterium Exchange Experiments—Amide hydrogen/deuterium exchange rates provide information about the amides buried in stable protein structures, which result in slow exchange rates at a second-level time scale. To understand how the dynamic behaviors in slow time scales are related to the structural stability of *Ef*-ACP, hydrogen/deuterium exchange experiments were performed, and the protection factors were calculated to obtain information about the degree of protection of protein amide protons against hydrogen/deuterium exchange. The first HSQC spectrum was acquired 5 min after the addition of D_2O to the protein. Many residues showed rapid exchange, and only 53 amide peaks among 78 remained after 10 min in the first HSQC spectrum. The helical regions of *Ef*-ACP with the exception of the short helix III had high protection factor values in the presence of Ca^{2+} (Fig. 6*A*). This implies that the residues in helices I, II, and IV were involved in stable folds unlike the residues in the other regions, and this result agrees well with the hNOE data. Although some residues, such as Phe^{18}, Ile^{20}, Gln^{24}, Leu^{29}, Ile^{31}, Lys^{32}, Asp^{34}, Leu^{35}, and Thr^{55}, were in the loop region, they showed high protection factors ($\log P > 2$). Fig. 6*B* shows the examples of fitting results of the slow hydrogen/deuterium-exchanging residues (Ser^{15}, Phe^{18}, Phe^{45}, and Phe^{53}). The exchange rates shown in Fig. 6*B* are 1.58×10^{-3} min^{-1} (Ser^{15}), 5.82×10^{-3} min^{-1} (Phe^{18}), 4.74×10^{-3} min^{-1} (Phe^{45}), and 1.15×10^{-3} min^{-1} (Phe^{53}). Although Phe^{18} is located in the $\alpha_1\alpha_2$ loop, the exchange rate is slow, resulting from a stable hydrophobic interaction with Phe^{45}. Phe^{53} plays important roles in hydrophobic interactions in the hydrophobic cleft of *Ef*-ACP, and its exchange rate ($1.15 \times$

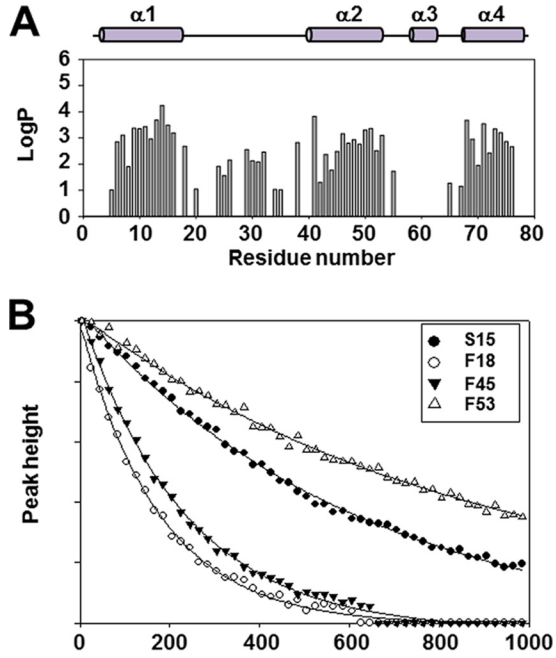

FIGURE 6. **Hydrogen/deuterium exchange experiment of *Ef*-ACP in the presence of Ca^{2+}.** *A*, the protection factor of *Ef*-ACP is depicted by a *bar graph* as a function of the residue sequence number of *Ef*-ACP. The *solid* and *filled bars above* the *plots* represent the four helices of *Ef*-ACP. *B*, time course of exchange showing signal loss due to hydrogen/deuterium exchange as a function of time after the addition of D_2O for each of the four residues. Peak height is in arbitrary units.

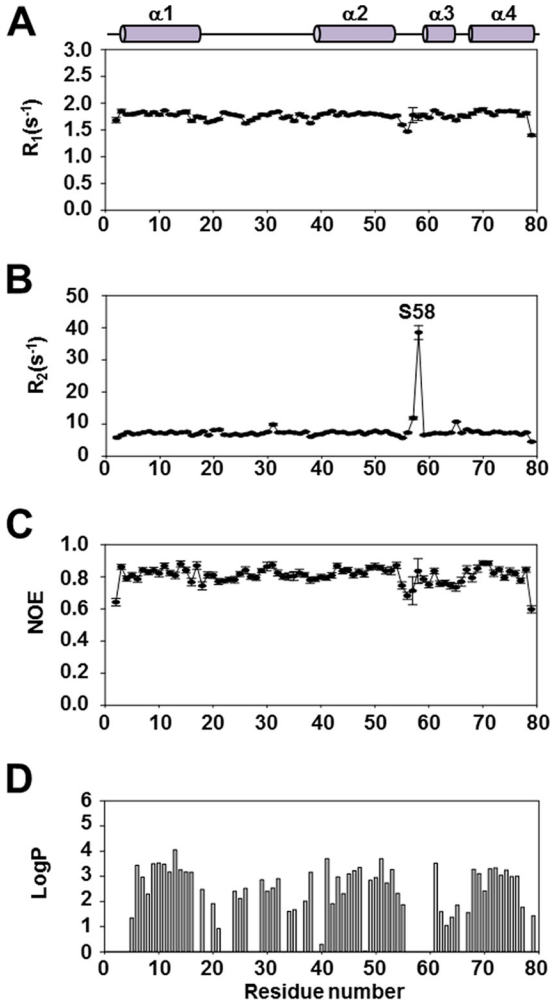

FIGURE 7. **Spin relaxation rates and Protection factor of *Ef*-ACP in the absence of Ca^{2+}.** The values of R_1 (*A*), R_2 (*B*), and the steady-state heteronuclear NOEs (*C*) are plotted as a function of the residue sequence number for *Ef*-ACP. *Above* the *plots*, the *solid* and *filled bars* represent the four helices of *Ef*-ACP. *D*, protection factor of *Ef*-ACP in the absence of Ca^{2+} depicted by a *bar graph* as a function of the residue sequence number of *Ef*-ACP. The *solid* and *filled bars above* the *plots* represent the four helices of *Ef*-ACP. All NMR data of *Ef*-ACP were measured at 298 K.

10^{-3} min^{-1}) is similar to the previously reported value of Phe^{50}, the corresponding residue in *Ec*-ACP (4.61×10^{-3} min^{-1}) (60). Hydrogen bonds between Ser^{15} and Ile^{20} result in slow exchange rate of the amide proton of Ile^{20} in the $\alpha_1\alpha_2$ loop as well. Amide protons of Gln^{24} and Leu^{29} form hydrogen bonds with Glu^{21} and Thr^{29}, respectively, and demonstrate slow hydrogen/deuterium exchange rates. *Ef*-ACP contains one turn from Ile^{31} to Leu^{35} in the $\alpha_1\alpha_2$ loop, resulting in the decrease of exchange rates of Ile^{31}, Lys^{32}, Asp^{34}, and Leu^{35}. Previous work on *Ec*-ACP has also reported that residues in the C-terminal portion from 26 to 34 in the $\alpha_1\alpha_2$ loop also exhibit greater protection factors than do residues at the N-terminal region of this loop (60). Hydrogen bonding interaction between Thr^{55} and Glu^{50} decreased the exchange rate of the amide proton of Thr^{55}. Even after 4 days, the *Ef*-ACP spectrum still showed many peaks for the residues located in helices I, II, and IV. These residues are Val^6, Leu^7, Val^{10}, Ala^{11}, Ile^{13}, and Ile^{14} in helix I; Val^{46}, Leu^{47}, Glu^{48}, Leu^{49}, Glu^{50}, and Phe^{53} in helix II; and Val^{68}, Ala^{71}, Val^{72}, Asp^{73}, Tyr^{74}, Ile^{75}, and Val^{76} in helix IV.

Effect of Ca^{2+} on Ef-ACP—To investigate the effect of Ca^{2+}, fast backbone dynamics were studied by measuring the R_1, R_2, and hNOEs of *Ef*-ACP in the absence of Ca^{2+} (Fig. 7, *A*–*C*). In the absence of Ca^{2+}, the average R_1, R_2, and hNOE values of *Ef*-ACP were 1.76 ± 0.021, 7.66 ± 0.15, and 0.81 ± 0.020 s^{-1}, which are very similar to those in the presence of Ca^{2+}. Similar to the data in the presence of Ca^{2+}, Ser^{58} in the $\alpha_2\alpha_3$ loop region showed high R_2 values, 38.49 ± 2.16 s^{-1} in the absence of Ca^{2+}, implying that they have conformational exchange in both conditions. The hydrogen/deuterium exchange rates in both conditions were also very similar (Figs. 6*A* and 7*D*), except over the short helix III region. In the case of metal-free conditions, helix III of *Ef*-ACP has higher protection compared with in conditions with Ca^{2+} ions. This may be because Asp^{61} and Glu^{63} in this helix may be the Ca^{2+} binding site and must be exposed to bind to Ca^{2+} ions, whereas in the absence of Ca^{2+}, they are buried inside and protected. Overall, the protection factors *of Ef*-ACP in both conditions are very similar. These results agree well with the thermal stability of *Ef*-ACP because the difference between T_m of *Ef*-ACP in the calcium-bound form and in the calcium-free form is only 6 °C.

Mutagenesis Studies of Ef-ACP—To assess the effects of specific residues on the thermal stability of *Ef*-ACP, site-directed mutagenesis was performed to generate five single-point mutations of *Ef*-ACP, S15G, H17A, F18A, F45A, and F53A, and their T_m values were determined using CD spectroscopy, as shown in Table 3. The T_m of the S15G mutant of *Ef*-ACP was 60.1 °C, 18.7 °C lower than that of the wild type protein, and the helical content was also much lower than that of the wild type *Ef*-ACP, implying that the hydrogen bond between Ser^{15} and Ile^{20} in the long $\alpha_1\alpha_2$ loop might be the key factor in stabilizing the confor-

TABLE 3
Melting temperatures of mutant *Ef*-ACPs in 25 mM MES buffer, pH 6.1, containing 5 mM $CaCl_2$

	Wild type	S15G	H17A	F18A	F45A	F53A
Melting temperature[a]	78.8 °C	60.1 °C	62.3 °C	69.5 °C	52.9 °C	54.7 °C

[a] Melting temperature was measured by CD spectroscopy.

mation. The T_m of the H17A mutant was 62.3 °C, 16.5 °C lower than that of the wild type, whereas its overall secondary structure was similar to that of wild type *Ef*-ACP. This implies that His^{17} might play an important role in conformational stabilization by reducing the electrostatic repulsion between the negatively charged residues but that mutation of His^{17} does not induce substantial conformational change. The T_m of F18A was also 9.3 °C lower than that of the wild type, and the helical content was a little lower than that of wild type ACP. In contrast, the T_m of the F45A mutant was 52.9 °C, 25.9 °C lower than that of the wild type, and the helical content of F45A mutant *Ef*-ACP was much lower than that of wild type *Ef*-ACP. The HSQC spectrum showed that F45A mutation caused partial unfolding of protein structure (data not shown). The mutations of Phe^{53} with alanine at F53A also exhibited a big influence (24.1 °C) on stability and on the *Ef*-ACP structure as well. These results imply that the hydrophobic interactions between Phe^{45} and Phe^{18}, as well as other hydrophobic interactions in the hydrophobic cleft, including those between Val^6, Phe^{53}, and Ile^{75}, play critical roles in the proper folding and structural stability of *Ef*-ACP. These results demonstrate that electrostatic as well as hydrophobic interactions in *Ef*-ACP are key factors in thermal and structural stability in *Ef*-ACP.

Discussion

To provide insights into understanding the thermal stability of *Ef*-ACP, we identify the key factors in its stability by investigating its structure, dynamics, and melting temperatures of mutants. In previous studies, *Ec*-ACP has been reported to exhibit higher melting temperatures (64.3 °C) in the presence of calcium ion compared with *Ec*-ACP in the absence of calcium ion (52.7 °C) (57). In addition, in the presence of calcium ion, *V. harveyi* ACP has an α-helical structure with a T_m of 66.4 °C; however, in the absence of calcium ion, this protein is unfolded (58). As shown in Fig. 9 (*A*–*C*), severe electrostatic repulsions exist in helix II and in the $\alpha_1\alpha_2$ loop near the metal binding site A in both *Ec*-ACP and *V. harveyi* ACP. The low thermal stability of *Ec*-ACP and *V. harveyi* ACP in conditions of the absence of calcium results from the severe electrostatic repulsion between negatively charged residues, which reduces the stability of *Ec*-ACP. In previous reports, the neutralization of acidic residues in helix II was shown to stabilize *V. harveyi* ACP conformation (12). In the case of *Ec*-ACP, His^{75} at helix IV retained a stable native conformation by shielding the electrostatic repulsion between negatively charged residues (59). Furthermore, *V. harveyi* ACP, which has an alanine instead of histidine at the C terminus, becomes unfolded, whereas the A75H mutation restores proper folding of the α-helical structures by reducing the electrostatic repulsion (58, 61, 62).

As shown in this study, *Ef*-ACP is more thermally stable than are other ACPs in the absence of calcium, and the thermal stabilities of *Ef*-ACP in calcium-bound (78.8 °C) and calcium-free conditions (72.5 °C) are only 6.3 °C different, which is a relatively small difference compared with other ACPs, as shown in Table 1. Also, the relaxation rates as well as hydrogen/deuterium exchange data of *Ef*-ACP are similar for both conditions. This may result from His^{17}, which is unique in *Ef*-ACP, at the end of the first helix. As shown in Fig. 9*C*, His^{17} in *Ef*-ACP reduced the electrostatic repulsion between negatively charged residues in the $\alpha_1\alpha_2$ loop and helix II. The H17A mutant was identified to have a 12 °C decrease in melting temperature. Because distribution of negatively charged residues in *Ef*-ACP is different from those of *Ec*-ACP and *V. harveyi* ACP, the metal binding sites of *Ef*-ACP might differ from those of other ACPs, which needs to be investigated in further studies.

Most type II ACPs have a flexible long $\alpha_1\alpha_2$ loop between helix I and helix II, resulting in low hNOEs and in the deuterium exchange experiment (4, 35, 59, 60). In addition, most ACPs, such as *Ec*-ACP, oxytetracycline-ACP, and frenolicin-ACP, have large amplitude motions and show lower NOE values in the $\alpha_1\alpha_2$ loop. The average hNOE value of the $\alpha_1\alpha_2$ loop in frenolicin-ACP is $0.49 \pm 0.038\ s^{-1}$, whereas that in *Ef*-ACP is $0.78 \pm 0.007\ s^{-1}$ (59, 63, 64). This loop rigidity results from the hydrogen bonds between the side chain oxygen of Ser^{15} in helix I and the backbone amide of Ile^{20} in the loop and a hydrophobic interaction between Phe^{18} ($\alpha_1\alpha_2$ loop) and Phe^{45} (helix II). As shown in Table 3, the T_m of the S15G mutant was 18 °C lower compared with that of wild type *Ef*-ACP, implying that this hydrogen bonding interaction is essential for the thermal stability of *Ef*-ACP.

Previous molecular dynamics simulations on *Ec*-ACP showed that there were two different acyl chain binding pockets, resulting in the splitting of the hydrophobic binding cavity (14). Subpocket I is located between helices II, III, and IV, and subpocket II is located more toward helix I, between helices I, II, and IV. The entrance of these pockets is close to the N-terminal end of helix II, which is near the prosthetic group binding site, at Ser^{36} in *Ec*-ACP. In *Ec*-ACP, a side chain reorientation of Leu^{42} and Leu^{46} is required to act as a switch to determine the direction of acyl chain binding between the two pockets (14). In contrast, for *Ef*-ACP, a hydrophobic interaction between Phe^{45} at helix II and Phe^{18} at the beginning of the $\alpha_1\alpha_2$ loop may block the entrance into subpocket II, which otherwise would accommodate the growing acyl chain between helices I, II, and IV as shown in Fig. 8.

Superimposing only the Cα atoms in *Ef*-ACP onto other type II ACPs gave root mean square deviation values of 2.62 Å for *Ec*-ACP, 2.38 Å for *M. tuberculosis* ACP, 3.24 Å for *P. falciparum* ACP, and 2.87 Å for *B. subtilis* ACP (32–34, 37). Sequence alignments shown in Fig. 1 indicated that the similarity between *Ef*-ACP and other ACPs was high (Gram-positive: *B. subtilis* ACP, 72.2%; *M. tuberculosis* ACP, 63.0%; and *S. aureus* ACP, 74.7%; Gram-negative: *Ec*-ACP, 69.6%; *Acinetobacter baumanni* ACP, 69.6%; *P. falciparum* ACP, 67.1%; and *V. harveyi* ACP, 68.4%). Comparisons of the structures of other ACPs with that of *Ef*-ACP indicate that they all have similar global folds with similar secondary structural elements, with the four-helix bundle fold being well conserved among ACPs (Fig. 9, *D*–*G*). In comparison with the *B. subtilis* ACP structure, the distinctive

difference between that of *Ef*-ACP appears at the $\alpha_2\alpha_3$ loop, which protrudes outward in the latter. The distance between the Cα of phosphopantethylated Ser^{39} and the Cα of Ser^{58} at the $\alpha_2\alpha_3$ loop was 16.6 Å, whereas the corresponding distances in *M. tuberculosis* ACP, *Ec*-ACP, *B. subtilis* ACP, and *P. falciparum* ACP are 12.9, 12.9, 13.5, and 14.4 Å, respectively. Therefore, this results in the outward movement of helix III to expand the hydrophobic cavity for stable binding of the growing acyl chains in *Ef*-ACP compared with other ACPs. Because Phe^{45}-mediated hydrophobic interaction may block the entrance into subpocket II in *Ef*-ACP, to accommodate the long growing acyl chain, Ser^{58} in the $\alpha_2\alpha_3$ loop of *Ef*-ACP might facilitate the movement of this flexible loop and of helix III further outside the main structure compared with other ACPs. The relaxation rates confirmed the flexibility of Ser^{58} in the $\alpha_2\alpha_3$ loop as well. The R_2 rates were uniform in all regions of *Ef*-ACP with the exception of the R_2 rates of Ile^{57} and Ser^{58}, implying the flexibility of the $\alpha_2\alpha_3$ loop in *Ef*-ACPs. Within the $\alpha_2\alpha_3$ loop of *Ec*-ACP, Ile^{54} and Pro^{55}, showed uniform R_2 value because proline had a tendency to form a rigid bent structure in the loop in our previous study (59). These results imply that the Ile^{57} and Ser^{58} loop region might have a conformational exchange to release and accept the acyl chain and generate enough room to accommodate the longer acyl chains.

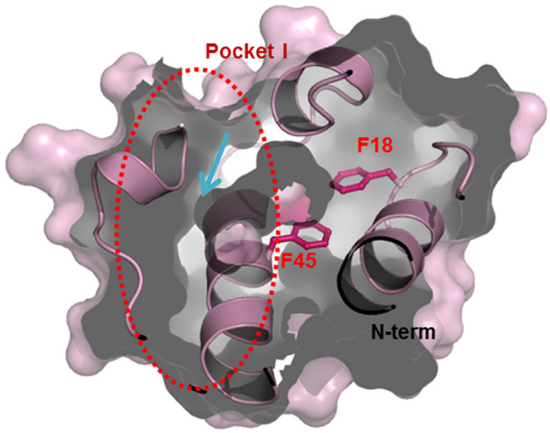

FIGURE 8. **Surface representation of subpockets in the hydrophobic cavity.** Phe^{45} in *Ef*-ACP has hydrophobic interactions with Phe^{18}, resulting in blockage of the entrance into the alternate binding cavity of *Ef*-ACP between helices I, II, and IV. The *arrows* represent the direction of the path of the growing acyl chain.

It has been reported that the $\alpha_2\alpha_3$ loop is important in interactions between ACP and FabA in fatty acid synthesis because perturbing the $\alpha_2\alpha_3$ loop is required for these protein-protein interactions (60). In previous studies, Ile^{54} in *Ec*-ACP, which corresponds to Ile^{57} in *Ef*-ACP, shows a large chemical shift perturbation in the ACP spectra by the addition of FabA (65). Here, conformational exchange in Ile^{57} and Ser^{58} in the $\alpha_2\alpha_3$ loop was observed for the first time, and the flexibility of the $\alpha_2\alpha_3$ loop might play an important role in its interaction with other FAS enzymes that could promote release of the growing acyl moieties from the hydrophobic pocket of ACP.

It has been reported that the Glu and Asp residues in helix II of *Ec*-ACP are important to recognize FabA, FabB, FabD, FabG, MCAT, AcpS, and FabH (61, 65–68). For example, Arg^{249} in the basic surface of FabH is critical for interaction with Glu^{41} of *Ec*-ACP (69). NMR and mutagenesis studies have shown that Glu^{41} and Glu^{48} in *E. coli* are important for FabG binding (67). Also, negatively charged residues in helix II of *Ec*-ACP have electrostatic interactions with basic residues of AcpS (70). Because *Ef*-ACP also has many negatively charged residues in helix II and suitable for binding with FAS proteins similar to *Ec*-ACP, molecules that mimic helix II and the $\alpha_2\alpha_3$ loop of *Ef*-ACP may inhibit these interactions with various FAS proteins and can be attractive candidates as therapeutic agents against drug-resistant strains of *E. faecalis*.

In conclusion, *Ef*-ACP has unique features, including hydrophobic interactions between Phe^{45} and Phe^{18} and hydrogen bonds between Ser^{15} and Ile^{20} in the $\alpha_1\alpha_2$ loop, resulting in the

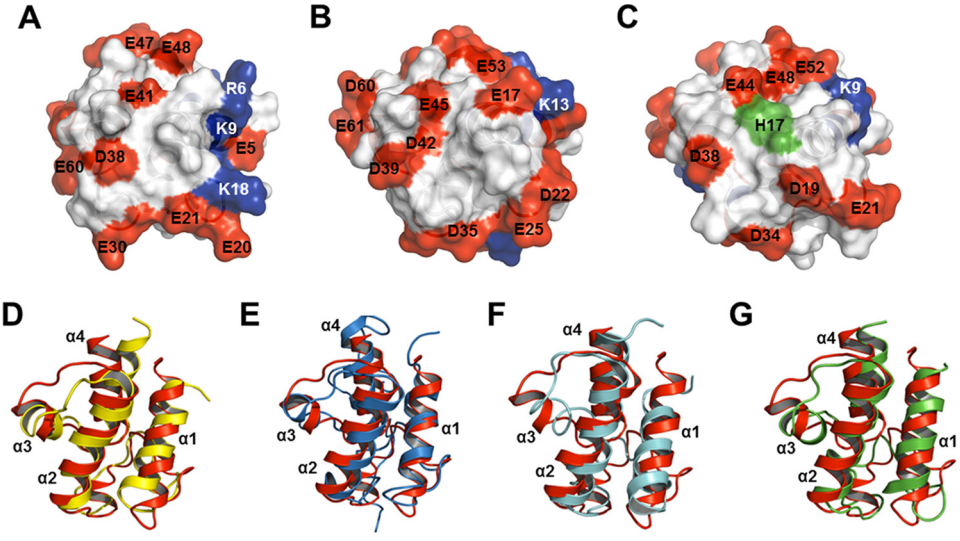

FIGURE 9. **Electrostatic potential surface structure and structural comparison of ACPs.** *A–C*, electrostatic potential of *Ec*-ACP (PDB entry 2K93) (*A*), *V. harveyi* ACP (PDB entry 2L0Q) (*B*), and *Ef*-ACP (PDB entry 2N50) (*C*). The residue numbers are *labeled*. Positive and negative charge residues are *colored* in *blue* and *red*, respectively. The His^{17} residue is *colored* in *green*. This surface structure is rotated about the *y* axis by 90° compared with that shown in Fig. 4*A*. *D–G*, structural comparison of *Ef*-ACP with other ACPs; overlay of structures of *Ef*-ACP (red; PDB entry 2N50) and *Ec*-ACP (*yellow*; PDB entry 2K93) (*D*), *Ef*-ACP and *M. tuberculosis* ACP (*blue*; PDB entry 1KIP) (*E*), *Ef*-ACP and *P. falciparum* ACP (*cyan*; PDB entry 2QF0) (*F*), and *Ef*-ACP and *B. subtilis* ACP (*green*; PDB entry 1HY8) (*G*). Each helix is *labeled* from $\alpha 1$ to $\alpha 4$, and this overlay structure has the same orientation as the structure shown in Fig. 4*A*.

high thermal stability of *Ef*-ACP. Furthermore, Ser^{58} in the $\alpha_2\alpha_3$ loop of *Ef*-ACP can provide loop flexibility and allow the provision of room to accommodate a longer acyl chain. Further studies on the structures and dynamics of acylated *Ef*-ACP will provide insight to understand the optimum length of the acyl chain bound in the hydrophobic pocket of *Ef*-ACP and to clarify the specific recognition mechanisms between acyl-ACP and functionally different enzyme partners in the FAS pathway. This study may provide insights to develop useful inhibitors for fatty acid synthesis as potent antibiotics against pathogenic drug-resistant strains.

Author Contributions—Y.-G. P. and Y. K. designed the study and wrote the paper. Y.-G. P., K.-W. J., E. B., G.-S. H., and M.-C. J. performed CD and NMR experiments and analyzed the data. Y. P. and H. S. cloned and purified the proteins. All authors reviewed the results and approved the final version of the manuscript.

Acknowledgments—We thank the High Field NMR Research Program of the Korea Basic Science Institute.

References

1. Uauy, R., Mena, P., and Rojas, C. (2000) Essential fatty acids in early life: structural and functional role. *Proc. Nutr. Soc.* **59,** 3–15
2. Cronan, J. E., Jr. (2004) The structure of mammalian fatty acid synthase turned back to front. *Chem. Biol.* **11,** 1601–1602
3. Cronan, J. E. (2006) Remarkable structural variation within fatty acid megasynthases. *Nat. Chem. Biol.* **2,** 232–234
4. Chan, D. I., and Vogel, H. J. (2010) Current understanding of fatty acid biosynthesis and the acyl carrier protein. *Biochem. J.* **430,** 1–19
5. White, S. W., Zheng, J., Zhang, Y. M., and Rock. (2005) The structural biology of type II fatty acid biosynthesis. *Annu. Rev. Biochem.* **74,** 791–831
6. Byers, D. M., and Gong, H. (2007) Acyl carrier protein: structure-function relationships in a conserved multifunctional protein family. *Biochem. Cell Biol.* **85,** 649–662
7. Cronan, J. E. (2014) The chain-flipping mechanism of ACP (acyl carrier protein)-dependent enzymes appears universal. *Biochem. J.* **460,** 157–163
8. Shen, B., Summers, R. G., Gramajo, H., Bibb, M. J., and Hutchinson, C. R. (1992) Purification and characterization of the acyl carrier protein of the *Streptomyces glaucescens* tetracenomycin C polyketide synthase. *J. Bacteriol.* **174,** 3818–3821
9. Geiger, O., Spaink, H. P., and Kennedy, E. P. (1991) Isolation of the *Rhizobium leguminosarum* NodF nodulation protein: NodF carries a 4′-phosphopantetheine prosthetic group. *J. Bacteriol.* **173,** 2872–2878
10. Heaton, M. P., and Neuhaus, F. C. (1994) Role of the D-alanyl carrier protein in the biosynthesis of D-alanyl-lipoteichoic acid. *J. Bacteriol.* **176,** 681–690
11. Issartel, J. P., Koronakis, V., and Hughes, C. (1991) Activation of *Escherichia coli* prohaemolysin to the mature toxin by acyl carrier protein-dependent fatty acylation. *Nature* **351,** 759–761
12. Gong, H., Murphy, A., McMaster, C. R., and Byers, D. M. (2007) Neutralization of acidic residues in helix II stabilizes the folded conformation of acyl carrier protein and variably alters its function with different enzymes. *J. Biol. Chem.* **282,** 4494–4503
13. Crosby, J., and Crump, M. P. (2012) The structural role of the carrier protein–active controller or passive carrier. *Nat. Prod. Rep.* **29,** 1111–1137
14. Chan, D. I., Stockner, T., Tieleman, D. P., and Vogel, H. J. (2008) Molecular dynamics simulations of the apo-, holo-, and acyl-forms of *Escherichia coli* acyl carrier protein. *J. Biol. Chem.* **283,** 33620–33629
15. Kuch, A., Willems, R. J. L., Werner, G., Coque, T. M., Hammerum, A. M., Sundsfjord, A., Klare, I., Ruiz-Garbajosa, P., Simonsen, G. S., van Luit-Asbroek, M., Hryniewicz, W., and Sadowy, E. (2012) Insight into antimicrobial susceptibility and population structure of contemporary human *Enterococcus faecalis* isolates from Europe. *J. Antimicrob. Chemother.* **67,** 551–558
16. Orr, K. E., Holliday, M. G., Jones, A. L., Robson, I., and Perry, J. D. (2002) Survival of enterococci during hospital laundry processing. *J. Hosp. Infect.* **50,** 133–139
17. Wade, J. J. (1997) *Enterococcus faecium* in hospitals. *Eur. J. Clin. Microbiol. Infect. Dis.* **16,** 113–119
18. Silva Laport, M., da Silva, M. R., Costa Silva, C., do Carmo de Freire Bastos, M., and Giambiagi-deMarval, M. (2003) Heat-resistance and heat-shock response in the nosocomial pathogen *Enterococcus faecium*. *Curr. Microbiol.* **46,** 313–317
19. Paulsen, I. T., Banerjei, L., Myers, G. S., Nelson, K. E., Seshadri, R., Read, T. D., Fouts, D. E., Eisen, J. A., Gill, S. R., Heidelberg, J. F., Tettelin, H., Dodson, R. J., Umayam, L., Brinkac, L., Beanan, M., Daugherty, S., DeBoy, R. T., Durkin, S., Kolonay, J., Madupu, R., Nelson, W., Vamathevan, J., Tran, B., Upton, J., Hansen, T., Shetty, J., Khouri, H., Utterback, T., Radune, D., Ketchum, K. A., Dougherty, B. A., and Fraser, C. M. (2003) Role of mobile DNA in the evolution of vancomycin-resistant *Enterococcus faecalis*. *Science* **299,** 2071–2074
20. Huycke, M. M., Sahm, D. F., and Gilmore, M. S. (1998) Multiple-drug resistant enterococci: the nature of the problem and an agenda for the future. *Emerg. Infect. Dis.* **4,** 239–249
21. Neely, A. N., and Maley, M. P. (2000) Survival of enterococci and staphylococci on hospital fabrics and plastic. *J. Clin. Microbiol.* **38,** 724–726
22. Seedat, J., Zick, G., Klare, I., Konstabel, C., Weiler, N., and Sahly, H. (2006) Rapid emergence of resistance to linezolid during linezolid therapy of an *Enterococcus faecium* infection. *Antimicrob. Agents Chemother.* **50,** 4217–4219
23. Kristich, C. J., Li, Y. H., Cvitkovitch, D. G., and Dunny, G. M. (2004) Esp-independent biofilm formation by *Enterococcus faecalis*. *J. Bacteriol.* **186,** 154–163
24. Brusic, V., and Petrovsky, N. (2005) Immunoinformatics and its relevance to understanding human immune disease. *Expert Rev. Clin. Immunol.* **1,** 145–157
25. Nallapareddy, S. R., Singh, K. V., Sillanpää, J., Zhao, M., and Murray, B. E. (2011) Relative contributions of Ebp Pili and the collagen adhesin ace to host extracellular matrix protein adherence and experimental urinary tract infection by *Enterococcus faecalis* OG1RF. *Infect. Immun.* **79,** 2901–2910
26. Arias, C. A., and Murray, B. E. (2008) Emergence and management of drug-resistant enterococcal infections. *Expert Rev. Anti Infect. Ther.* **6,** 637–655
27. Murray, B. E. (1990) The life and times of the *Enterococcus*. *Clin. Microbiol. Rev.* **3,** 46–65
28. Vergis, E. N., Hayden, M. K., Chow, J. W., Snydman, D. R., Zervos, M. J., Linden, P. K., Wagener, M. M., Schmitt, B., and Muder, R. R. (2001) Determinants of vancomycin resistance and mortality rates in enterococcal bacteremia. a prospective multicenter study. *Ann. Intern. Med.* **135,** 484–492
29. Lee, J. Y., Jeong, K. W., Shin, S., Lee, J. U., and Kim, Y. (2012) Discovery of novel selective inhibitors of *Staphylococcus aureus* β-ketoacyl acyl carrier protein synthase III. *Eur. J. Med. Chem.* **47,** 261–269
30. Jeong, K. W., Lee, J. Y., Kang, D. I., Lee, J. U., Shin, S. Y., and Kim, Y. (2009) Screening of flavonoids as candidate antibiotics against *Enterococcus faecalis*. *J. Nat. Prod.* **72,** 719–724
31. Holak, T. A., Kearsley, S. K., Kim, Y., and Prestegard, J. H. (1988) Three-dimensional structure of acyl carrier protein determined by NMR pseudoenergy and distance geometry calculations. *Biochemistry* **27,** 6135–6142
32. Wu, B. N., Zhang, Y. M., Rock, C. O., and Zheng, J. J. (2009) Structural modification of acyl carrier protein by butyryl group. *Protein Sci.* **18,** 240–246
33. Xu, G. Y., Tam, A., Lin, L., Hixon, J., Fritz, C. C., and Powers, R. (2001) Solution structure of *B. subtilis* acyl carrier protein. *Structure* **9,** 277–287
34. Wong, H. C., Liu, G., Zhang, Y. M., Rock, C. O., and Zheng, J. (2002) The solution structure of acyl carrier protein from *Mycobacterium tuberculosis*. *J. Biol. Chem.* **277,** 15874–15880
35. Park, S. J., Kim, J. S., Son, W. S., and Lee, B. J. (2004) pH-induced confor-

mational transition of *H. pylori* acyl carrier protein: insight into the unfolding of local structure. *J. Biochem.* **135,** 337–346
36. Barnwal, R. P., Van Voorhis, W. C., and Varani, G. (2011) NMR structure of an acyl-carrier protein from *Borrelia burgdorferi*. *Acta Crystallogr. Sect. F Struct. Biol. Cryst. Commun.* **67,** 1137–1140
37. Sharma, A. K., Sharma, S. K., Surolia, A., Surolia, N., and Sarma, S. P. (2006) Solution structures of conformationally equilibrium forms of holo-acyl carrier protein (PfACP) from *Plasmodium falciparum* provides insight into the mechanism of activation of ACPs. *Biochemistry* **45,** 6904–6916
38. Lim, J., Kong, R., Murugan, E., Ho, C. L., Liang, Z. X., and Yang, D. (2011) Solution structures of the acyl carrier protein domain from the highly reducing type I iterative polyketide synthase CalE8. *PLoS One* **6,** e20549
39. Perez, D. R., Leibundgut, M., and Wider, G. (2015) Interactions of the acyl chain with the *Saccharomyces cerevisiae* acyl carrier protein. *Biochemistry* **54,** 2205–2213
40. Płoskoń, E., Arthur, C. J., Evans, S. E., Williams, C., Crosby, J., Simpson, T. J., and Crump, M. P. (2008) A mammalian type I fatty acid synthase acyl carrier protein domain does not sequester acyl chains. *J. Biol. Chem.* **283,** 518–528
41. Zhang, Y. M., Marrakchi, H., White, S. W., and Rock, C. O. (2003) The application of computational methods to explore the diversity and structure of bacterial fatty acid synthase. *J. Lipid Res.* **44,** 1–10
42. Lambalot, R. H., and Walsh, C. T. (1995) Cloning, overproduction, and characterization of the *Escherichia coli* holo-acyl carrier protein synthase. *J. Biol. Chem.* **270,** 24658–24661
43. Rock, C. O., Cronan, J. E., Jr., and Armitage, I. M. (1981) Molecular properties of acyl carrier protein derivatives. *J. Biol. Chem.* **256,** 2669–2674
44. Delaglio, F., Grzesiek, S., Vuister, G. W., Zhu, G., Pfeifer, J., and Bax, A. (1995) NMRPipe: a multidimensional spectral processing system based on UNIX pipes. *J. Biomol. NMR* **6,** 277–293
45. Goddard, T. D., and Kneller, D. G. (2004) *SPARKY* 3, University of California, San Francisco
46. Cordier, F., Dingley, A. J., and Grzesiek, S. (1999) A doublet-separated sensitivity-enhanced HSQC for the determination of scalar and dipolar one-bond J-couplings. *J. Biomol. NMR* **13,** 175–180
47. Shen, Y., Delaglio, F., Cornilescu, G., and Bax, A. (2009) TALOS+: a hybrid method for predicting protein backbone torsion angles from NMR chemical shifts. *J. Biomol. NMR* **44,** 213–223
48. Güntert, P., Mumenthaler, C., and Wüthrich, K. (1997) Torsion angle dynamics for NMR structure calculation with the new program DYANA. *J. Mol. Biol.* **273,** 283–298
49. Güntert, P. (2004) Automated NMR structure calculation with CYANA. *Methods Mol. Biol.* **278,** 353–378
50. Laskowski, R. A., Rullmannn, J. A., MacArthur, M. W., Kaptein, R., and Thornton, J. M. (1996) AQUA and PROCHECK-NMR: programs for checking the quality of protein structures solved by NMR. *J. Biomol. NMR* **8,** 477–486
51. Koradi, R., Billeter, M., and Wüthrich, K. (1996) MOLMOL: a program for display and analysis of macromolecular structures. *J. Mol. Graph.* **14,** 51–55, 29–32
52. Farrow, N. A., Muhandiram, R., Singer, A. U., Pascal, S. M., Kay, C. M., Gish, G., Shoelson, S. E., Pawson, T., Forman-Kay, J. D., and Kay, L. E. (1994) Backbone dynamics of a free and phosphopeptide-complexed Src homology 2 domain studied by ^{15}N NMR relaxation. *Biochemistry* **33,** 5984–6003
53. Jeong, K. W., Kang, D. I., Lee, E., Shin, A., Jin, B., Park, Y. G., Lee, C. K., Kim, E. H., Jeon, Y. H., Kim, E. E., and Kim, Y. (2014) Structure and backbone dynamics of vanadate-bound PRL-3: comparison of ^{15}N nuclear magnetic resonance relaxation profiles of free and vanadate-bound PRL-3. *Biochemistry* **53,** 4814–4825
54. Lee, J., Jeong, K. W., Jin, B., Ryu, K. S., Kim, E. H., Ahn, J. H., and Kim, Y. (2013) Structural and dynamic features of cold-shock proteins of *Listeria monocytogenes*, a psychrophilic bacterium. *Biochemistry* **52,** 2492–2504
55. Bai, Y., Milne, J. S., Mayne, L., and Englander, S. W. (1993) Primary structure effects on peptide group hydrogen exchange. *Proteins* **17,** 75–86
56. Frederick, A. F., Kay, L. E., and Prestegard, J. H. (1988) Location of divalent ion sites in acyl carrier protein using relaxation perturbed 2D NMR. *FEBS Lett.* **238,** 43–48
57. Horvath, L. A., Sturtevant, J. M., and Prestegard, J. H. (1994) Kinetics and thermodynamics of thermal denaturation in acyl carrier protein. *Protein Sci.* **3,** 103–108
58. Chan, D. I., Chu, B. C., Lau, C. K., Hunter, H. N., Byers, D. M., and Vogel, H. J. (2010) NMR solution structure and biophysical characterization of *Vibrio harveyi* acyl carrier protein A75H: effects of divalent metal ions. *J. Biol. Chem.* **285,** 30558–30566
59. Kim, Y., Kovrigin, E. L., and Eletr, Z. (2006) NMR studies of *Escherichia coli* acyl carrier protein: dynamic and structural differences of the apo- and holo-forms. *Biochem. Biophys. Res. Commun.* **341,** 776–783
60. Andrec, M., Hill, R. B., and Prestegard, J. H. (1995) Amide exchange rates in *Escherichia coli* acyl carrier protein: correlation with protein structure and dynamics. *Protein Sci.* **4,** 983–993
61. Flaman, A. S., Chen, J. M., Van Iderstine, S. C., and Byers, D. M. (2001) Site-directed mutagenesis of acyl carrier protein (ACP) reveals amino acid residues involved in ACP structure and acyl-ACP synthetase activity. *J. Biol. Chem.* **276,** 35934–35939
62. Keating, M. M., Gong, H., and Byers, D. M. (2002) Identification of a key residue in the conformational stability of acyl carrier protein. *Biochim. Biophys. Acta* **1601,** 208–214
63. Li, Q., Khosla, C., Puglisi, J. D., and Liu, C. W. (2003) Solution structure and backbone dynamics of the holo form of the frenolicin acyl carrier protein. *Biochemistry* **42,** 4648–4657
64. Findlow, S. C., Winsor, C., Simpson, T. J., Crosby, J., and Crump, M. P. (2003) Solution structure and dynamics of oxytetracycline polyketide synthase acyl carrier protein from *Streptomyces rimosus*. *Biochemistry* **42,** 8423–8433
65. Nguyen, C., Haushalter, R. W., Lee, D. J., Markwick, P. R., Bruegger, J., Caldara-Festin, G., Finzel, K., Jackson, D. R., Ishikawa, F., O'Dowd, B., McCammon, J. A., Opella, S. J., Tsai, S. C., and Burkart, M. D. (2014) Trapping the dynamic acyl carrier protein in fatty acid biosynthesis. *Nature* **505,** 427–431
66. Worsham, L. M., Earls, L., Jolly, C., Langston, K. G., Trent, M. S., and Ernst-Fonberg, M. L. (2003) Amino acid residues of *Escherichia coli* acyl carrier protein involved in heterologous protein interactions. *Biochemistry* **42,** 167–176
67. Zhang, Y. M., Wu, B., Zheng, J., and Rock, C. O. (2003) Key residues responsible for acyl carrier protein and β-ketoacyl-acyl carrier protein reductase (FabG) interaction. *J. Biol. Chem.* **278,** 52935–52943
68. Arthur, C. J., Williams, C., Pottage, K., Płoskoń, E., Findlow, S. C., Burston, S. G., Simpson, T. J., Crump, M. P., and Crosby, J. (2009) Structure and malonyl CoA-ACP transacylase binding of *Streptomyces coelicolor* fatty acid synthase acyl carrier protein. *ACS Chem. Biol.* **4,** 625–636
69. Zhang, Y. M., Rao, M. S., Heath, R. J., Price, A. C., Olson, A. J., Rock, C. O., and White, S. W. (2001) Identification and analysis of the acyl carrier protein (ACP) docking site on β-ketoacyl-ACP synthase III. *J. Biol. Chem.* **276,** 8231–8238
70. Parris, K. D., Lin, L., Tam, A., Mathew, R., Hixon, J., Stahl, M., Fritz, C. C., Seehra, J., and Somers, W. S. (2000) Crystal structures of substrate binding to *Bacillus subtilis* holo-(acyl carrier protein) synthase reveal a novel trimeric arrangement of molecules resulting in three active sites. *Structure* **8,** 883–895